Experimental Analysis of Propeller Forces and Moments at High Angle of Incidence

Yuchen Leng, Thierry Jardin, Murat Bronz, Jean-Marc Moschetta

▶ **To cite this version:**

Yuchen Leng, Thierry Jardin, Murat Bronz, Jean-Marc Moschetta. Experimental Analysis of Propeller Forces and Moments at High Angle of Incidence. AIAA Scitech 2019 Forum, Jan 2019, San Diego, United States. 10.2514/6.2019-1331 . hal-01979061

HAL Id: hal-01979061

https://enac.hal.science/hal-01979061

Submitted on 19 Oct 2021

HAL is a multi-disciplinary open access archive for the deposit and dissemination of scientific research documents, whether they are published or not. The documents may come from teaching and research institutions in France or abroad, or from public or private research centers.

L'archive ouverte pluridisciplinaire **HAL**, est destinée au dépôt et à la diffusion de documents scientifiques de niveau recherche, publiés ou non, émanant des établissements d'enseignement et de recherche français ou étrangers, des laboratoires publics ou privés.

Open Archive Toulouse Archive Ouverte (OATAO)

OATAO is an open access repository that collects the work of some Toulouse researchers and makes it freely available over the web where possible.

This is an author's version published in: https://oatao.univ-toulouse.fr/28399

Official URL: https://doi.org/10.2514/6.2019-1331

To cite this version :

Leng, Yuchen and Jardin, Thierry and Bronz, Murat and Moschetta, Jean-Marc Experimental Analysis of Propeller Forces and Moments at High Angle of Incidence. (2019) In: AIAA Scitech 2019 Forum, 7 January 2019 - 11 January 2019 (San Diego, United States).

Any correspondence concerning this service should be sent to the repository administrator: tech-oatao@listes-diff.inp-toulouse.fr

Experimental Analysis of Propeller Forces and Moments at High Angle of Incidence

Yuchen Leng * Thierry Jardin † Murat Bronz ‡
and Jean-Marc Moschetta §

ISAE-SUPAERO, Université de Toulouse, France

ENAC, Toulouse, France

An experimental measurement on propeller forces and moments at high incidence was introduced. Test apparatus and data reduction process was discussed. Two sets of propellers were tested in SaBRe low speed wind tunnel: Graupner E-prop was used to validate the test-bench against known experiment; The second case, consisting of 3D-printed propellers, demonstrated variations in propeller aerodynamic efforts produced at high incidence angle for various advance ratios and blade pitch angles. The test also highlighted the importance of 3 dimensional effects such as stall delay in estimating propeller forces and moments at high incidence angle.

I. Introduction

With the advance of electric propulsion technologies, convertible aircraft that are capable of Vertical Take-Off and Landing (VTOL) have gained renewed interest thanks to its flexibility at constrained mission environment. Several concepts of convertible aircraft have been proposed; Airbus and Uber have recently revealed VTOL concepts aiming at future urban transportation in congested areas. Unmanned aerial vehicles, such as MAVION developed

*Ph.D. Candidate at ISAE/DAEP, and Research Engineer at DELAIR, 10 Avenue Edouard Belin, Toulouse, France

†Research Scientist, Département d'Aérodynamique, Energétique et Propulsion, Institut Supérieur de l'Aéronautique et de l'Espace, 10 Avenue Edouard Belin, Toulouse, France

‡Assistant Professor, UAV Lab, École Nationale de l'Aviation Civile, 7 Avenue Edouard Belin, Toulouse, France

§Professor, ISAE, Département d'Aérodynamique, Energétique et Propulsion, Institut Supérieur de l'Aéronautique et de l'Espace, 10 Avenue Edouard Belin, Toulouse, France

at ISAE[1] or Cyclone from ENAC, have demonstrated operational advantages in its convenience of recovery. To fully exploit the potential of VTOL operations, the dynamics during transition flight between hover and cruise is critical.[2] Apart from complex aerodynamic phenomena presented over lifting surfaces, propellers also experience large incidence angle up to 90° at unusual attitude. Operating away from design conditions, the propeller produces extra non-symmetrical forces and moments that greatly affect transition flight characteristics.[3]

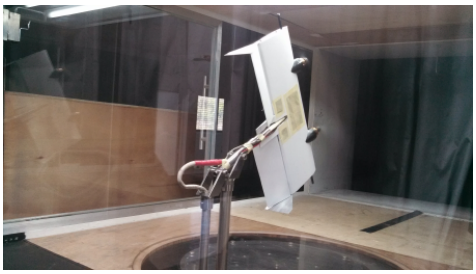

(a) ISAE MAVION[2]

(b) ENAC Cyclone[4]

Figure 1: VTOL aircraft concepts

A. Background

Propeller working in non-axial condition has been studied experimentally in aeronautical community. During 1950s, with the development of VTOL aircraft, several propeller tests have been performed at NASA research centres. Kuhn et al[5] investigated a four-propeller wing combination intended for a tilt-wing design. The tests were conducted in NASA Langley MPH 300 7- by 10-foot tunnel with a semi-span scaled model. The propeller-wing combination can be rotated to simulate angle of attack from 0° to 90°. Isolated propeller cases were also studied, and focused on the quasi-linear increase of normal force and pitch moment. Notably, pitch moment nearly doubled its value at some cases with wing attached. The authors attributed this effect to the non-uniform inflow between upper and lower wing surface. Yaw moment wasn't discussed since it was expected to be cancelled by rotating the pair of propellers in opposite directions.

In 1960, Yaggy et al[6] conducted a full-scale experiment of three propellers in NASA Ames 40- by 80-foot wind tunnel with incidence angle from 0° up to 85°. The three propellers were selected for an hypothetical manned VTOL aircraft. Blade pitch and advance ratio were varied during the test to investigate their influences. Thrust, torque, normal force, yaw and pitch moments were measured by balances isolated from motor. Yaw and pitch moments weren't measured for the third propeller due to its articulation mechanism. Data suggested an increase in thrust and torque from axial condition at the same advance ratio. Further more, normal force, yaw and pitch moment increased quasi-linearly with incidence angle.

In recent years, the growing interest in micro aerial vehicle has inspired more experimental

studies on propeller at high incidence. Theys et al[7] have tested a commercial propeller in the wind tunnel at the University of Liège. The propeller was supported on a turntable allowing incidence angle to be varied from 0° to 180°. Below 90° angle of incidence, the propeller showed similar behaviour to the experiments at larger scale. However, a drastic increase in pitch moment was measured near 90°. Maximum value of aerodynamic efforts were recorded beyond 90° incidence.

B. Present Work

The present study focused on high-incidence conditions encountered by a propeller during transition flight of a micro aerial vehicle. Besides providing data for understanding of propeller behaviour during transition flight, the experiment was conducted in hope of validating a newly developed reduced-order propeller analysis code.

In section II, the experiment set-up in ISAE low Reynolds number SaBRe wind tunnel is presented, followed by a description on data reduction process.

Section III presents the test bench validation under the same condition in Theys' research.

The last part of this paper shows data from test cases using 3D printed propellers. They were custom built to allow calculations on exact propeller geometry. The experimental data has been compared against numerical results from reduced-order propeller model.

II. Experiment Set-Up

An explanation of propeller test bench is presented in this section to provide a complete understanding of the mechanisms and effects involved in the measurement. Exact arrangement of experiment equipments are presented first, followed by necessary methods to compensate mass and structural aerodynamic effects.

A. Description of Apparatus

The measurement system was installed at ISAE low Reynolds number wind tunnel SaBRe, which is a closed circuit low-turbulence design with a $1.2m \times 0.8m$ test section. The propeller-motor assembly was supported by a movable mast installed from the test section ceiling. The metal mast itself was driven by an actuator which allowed the entire system to rotate about its vertical axis by 180° in either direction, simulating the variation of incidence angle.

At the lower tip of the mast, a custom-designed five-component balance was mounted both as a structural connection to the propeller-motor assembly and as the sensor to measure loads transferred from the assembly below. The balance wasn't sensitive to force measurement along its longitude axis. The installation is chosen to minimize negative impact and is further discussed in section B.

In this set-up, the aerodynamic loads on the propeller were not isolated from external disturbances, and have to be separated out through post-process, which will be discussed in section C.

A brushless motor was installed just below the balance loading end, and its rotation axis was determined to be $65mm$ lower the balance centre of measurement. In front of the motor, test propeller is fixed to the motor spinner. The test bench is shown in figure 2.

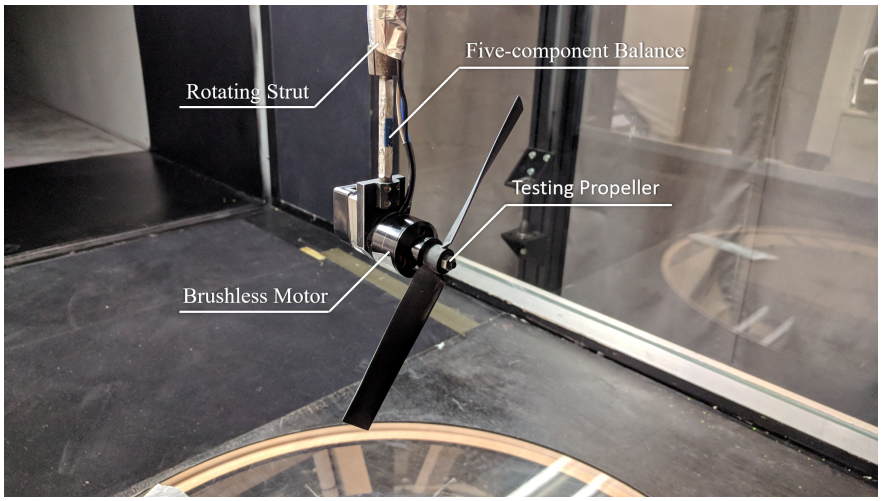

Figure 2: Propeller Test-Bench inside ISAE SaBRe Wind Tunnel

B. Coordinate System Convention

To describe the propeller assembly movement and the transformation from centre of measurement to propeller centre, a clear definition of coordinate system is required.

Two coordinates are used. Propeller frame, denoted with subscript $_p$, has its origin O_p at the propeller centre. Its z-axis is defined to be the axis of rotation, x-axis vertically points towards the ground and y-direction is determined by right-hand rule.

The balance frame, denoted by subscript $_b$ has the same orientation as the propeller system, but is situated at the balance centre of measurement, which is located $65mm$ above, and $40mm$ behind the base of propeller mount. The geometric relation between two coordinates is illustrated in figure 3.

The definition of all propeller aerodynamic loads are presented in figure 4 following the convention of propeller coordinate.

The angle between wind direction and propeller axis of rotation is the incidence angle, which can be set to a value between $0°$ and $180°$ through the rotation of mast. During a change of incidence, two coordinate systems rotates together without relative motion.

The six forces and moments acting on the propeller are decomposed following aircraft convention for rotor installed along longitudinal axis: T and Q, aligned with freestream, are

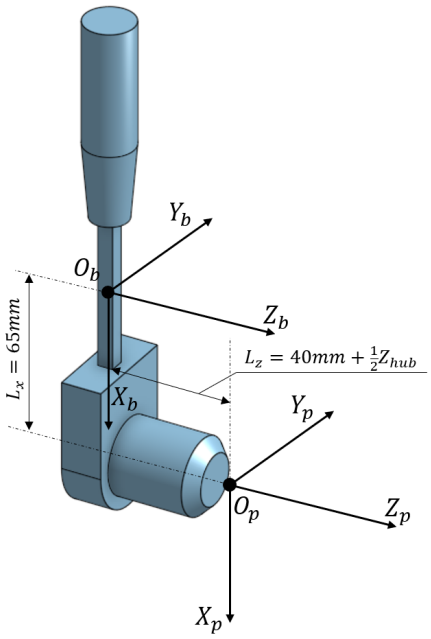

Figure 3: Balance and propeller coordinates

thrust and torque; Y and p, aligned with X_p-axis, are side force and pitching moment; N and n are normal force and yaw moment in Y_p-axis.

As mentioned before, the balance used for measurement is only sensitive in five components, namely two forces and three moments along a orthogonal coordinate. Based on previous studies,[3,6,8] side force Y is negligible and thus its insensitive axis is aligned with X_b-axis.

C. Compensation of External Disturbances

The force measurement from 5-component balance contains several external effects apart from propeller aerodynamic efforts, and thus must be compensated to obtain propeller loads. The external disturbances are categorised as following.

1. Static mass effects

The first component is resulted from the mass of test bench and propeller-motor assembly. Denoted by subscript $_0$, this component is measured for each propeller at various incidence angles. In the general form it contains five components, and its variation with incidence angle is caused by the slight alignment error in balance installation, which is derived in appendix I.

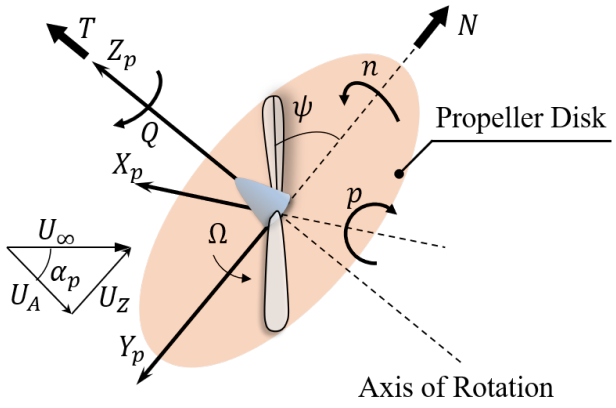

Figure 4: Aerodynamic loads on a propeller at incidence

$$\begin{bmatrix} \vec{F}_0 \\ \vec{M}_0 \end{bmatrix} = \begin{bmatrix} F_{y0} \\ F_{z0} \\ M_{x0} \\ M_{y0} \\ M_{z0} \end{bmatrix}$$

2. Static aerodynamic effects

The second component is the aerodynamic efforts produced by structures other than the propeller, and is denoted by subscript $_{aero}$. The structures contains mainly of cylinder geometries, and thus airflow around those structures should be sufficiently separated at testing speeds such that Reynolds number effect is negligible.[9] This component is obtained through two measurements. Firstly, with propeller uninstalled and $V_\infty = 0$, the motor mass effect F_{m0} and M_{m0} are measured at various incidence angle. The wind-tunnel is subsequently run at test speed and acquisitions of F_m^* and M_m^* are made at corresponding incidence angles. The aerodynamic load is further derived as the difference between these two measurements.

$$\begin{bmatrix} \vec{F}_{aero} \\ \vec{M}_{aero} \end{bmatrix} = \begin{bmatrix} \vec{F}_m^* \\ \vec{M}_m^* \end{bmatrix} - \begin{bmatrix} \vec{F}_{m0} \\ \vec{M}_{m0} \end{bmatrix}$$

To compensate the influence of atmosphere condition on dynamic pressure, the aerodynamic disturbances are further scaled by measured dynamic pressure.

$$\begin{bmatrix} \vec{C}_{F_{aero}} \\ \vec{C}_{M_{aero}} \end{bmatrix} = \frac{2}{\rho V_\infty^2} \begin{bmatrix} \vec{F}_{aero} \\ \vec{M}_{aero} \end{bmatrix}$$

3. Compensation of measurement

To obtain the propeller aerodynamic forces and moments, those two external disturbances are subtracted from the raw data measured at the centre of measurement (F_b^*, M_b^*). The static aerodynamic effects are scaled with measured dynamic pressure before compensation.

$$\begin{bmatrix} \vec{F}_b \\ \vec{M}_b \end{bmatrix} = \begin{bmatrix} \vec{F}_b^* \\ \vec{M}_b^* \end{bmatrix} - \begin{bmatrix} \vec{F}_0 \\ \vec{M}_0 \end{bmatrix} - \frac{1}{2}\rho V_\infty^2 \begin{bmatrix} \vec{C}_{Faero} \\ \vec{C}_{Maero} \end{bmatrix}$$

4. Transformation to propeller centre

To obtain aerodynamic efforts at the propeller centre, ie the origin of propeller coordinate, the compensated forces and moments should be transformed. Following the test bench convention in figure 3, the transform matrix can be found as following.

$$\begin{bmatrix} \vec{F}_p \\ \vec{M}_p \end{bmatrix} = \begin{bmatrix} 1 & 0 & 0 & 0 & 0 \\ 0 & 1 & 0 & 0 & 0 \\ -L_z & 0 & 1 & 0 & 0 \\ 0 & -L_x & 0 & 1 & 0 \\ L_x & 0 & 0 & 0 & 1 \end{bmatrix} \begin{bmatrix} \vec{F}_b \\ \vec{M}_b \end{bmatrix}$$

where L_x and L_z are the moment arm from centre of measurement to the propeller centre in x and z direction, respectively. It is assumed that, after compensation of mass effect, force in the x direction is negligible.

III. Validation of Test bench

A 9-inch Graupner E-prop was first tested to compare with experiments conducted by Theys, et al[8] under similar conditions for validation. The propeller was operated at various rotation speed and freestream velocity combinations detailed in the table 1.

Rotation Speed (RPM)	Freestream Velocity (m/s)	
4000	3	6
4500	3	6

Table 1: E-prop Test Matrix

The five components obtained from experiment were compared with values from Theys at similar rotation speeds, namely, thrust T, normal force N, pitching moment p, yaw moment n and torque Q. All results are presented for incidence angle from 0° to 90° by an interval of 30°, and are in the form of non-dimensional coefficients defined below.

$$C_T = \frac{T}{\rho \left(\Omega/2\pi\right)^2 D^4} \qquad C_Q = \frac{Q}{\rho \left(\Omega/2\pi\right)^2 D^5}$$
$$C_N = \frac{N}{\rho \left(\Omega/2\pi\right)^2 D^4} \qquad C_n = \frac{n}{\rho \left(\Omega/2\pi\right)^2 D^5}$$

where Ω is rotation speed in radian per second and D is propeller diameter.

Figure 5 gives results on thrust and torque. The curves from ISAE experiment share similar trend with Theys. At constant rotational speed, the thrust and torque coefficients increase with incidence angle, and reach peak value beyond 90°

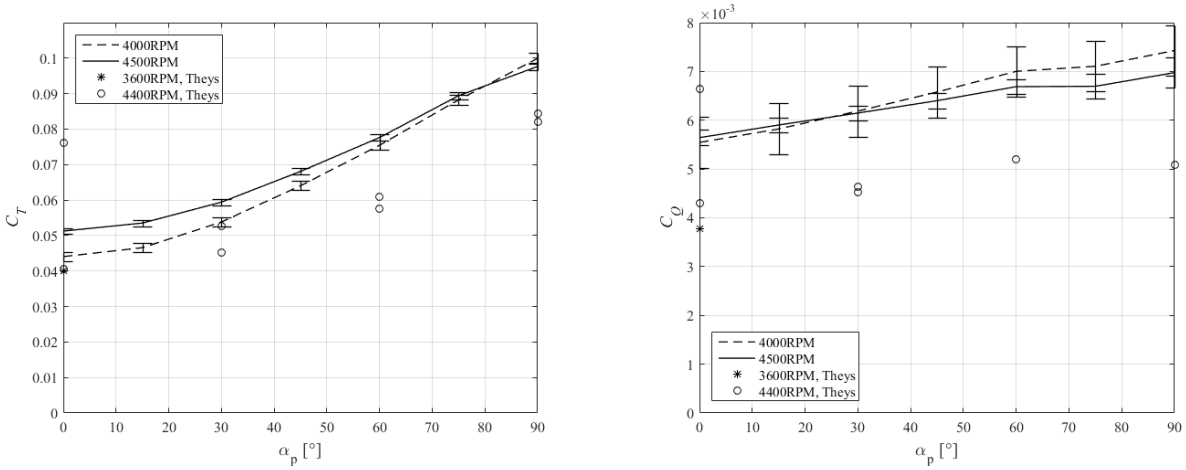

(a) Thrust coefficient C_T (b) Torque coefficient C_Q

Figure 5: Comparison of thrust and torque measurements on E-prop

An overestimation can be observed when compared with Theys' data. The discrepancy is highly likely due to the difficulty in matching rotor rotational speed. Theys et al controlled rotor by constant voltage input, and thus rotational speed varies slightly with incidence angle. In general, the propeller rotated at a higher speed than the comparison case, producing larger thrust and torque coefficients.

Non-symmetrical forces and moments are presented in figure 6 and 7.

In figure 6, two major non-symmetrical components in oblique propeller flow are presented. The normal force is the component in rotor disk plane, which increases with α_p until around 60°. The measurement from two experiments agree well in the tested range.

The yaw moment measurement largely agree with data from Theys. The data suggests a quasi-linear increase in yaw moment till around 60°. The asymmetrical moment levels off thereafter at around 90°, and a slightly larger value is observed compared to Theys.

Figure 7 shows the variation in pitching moment, the supposedly secondary asymmetrical load on propeller. Here, current measurement is again consistent with Theys' data, suggest-

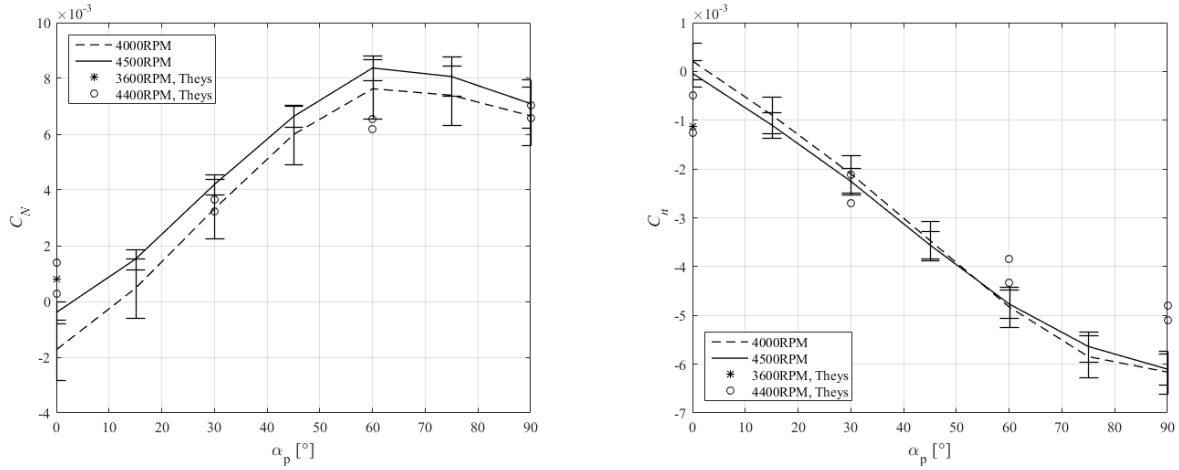

(a) Normal force coefficient C_N (b) Yaw moment coefficient C_n

Figure 6: Comparison of normal force and yaw moment measurements on E-prop

ing there is a significant pitching moment increase at high incidence angle. The variation begins a shallow rise from zero up to around 60°, where a sharp increase follows.

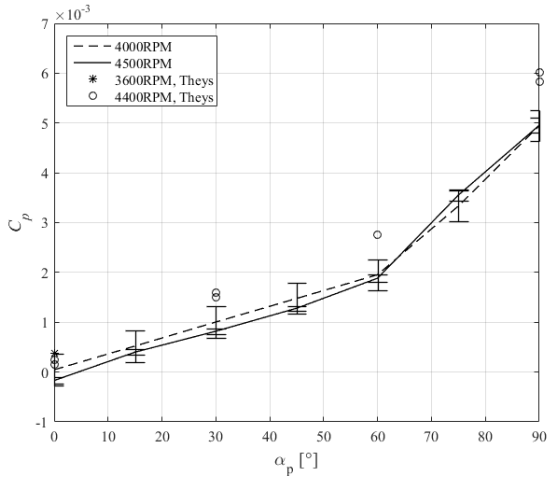

Figure 7: Comparison of pitching moment measurements on E-prop

The origin of pitching is likely due to 3 dimensional effects when blades are nearly aligned with flow direction. It may be further analysed by comparing phase shift to yaw moment. The phenomena may be roughly simulated through pressure distribution on a circular wing.[10]

The comparison, although not exact, demonstrates the validity of propeller test bench in ISAE-SaBRe wind tunnel in providing credible force and moment measurement for a propeller at high incidence angle. Data acquired from the balance captures principle variation in propeller aerodynamic loads and is accurate for qualitative analysis at practical range.

The major deficiency lies in the system is the residual drift which restricts small normal force N measurement.

IV. NACA Propeller Test

To validate a reduced-order Blade Element Theory (BET) model developed at ISAE-Supaéro, a series of simplified propellers denoted as NACA were manufactured using 3D printer. They feature a constant chord and NACA0012 blade section profile. The twist distribution is given as $\beta = \tan^{-1}\frac{C}{\bar{r}}$, where $C = \tan\beta_{tip}$ and $\bar{r}$ is fractional radius. The propellers are of different pitch by changing tip blade angle β_{tip}. Current tests covered propellers with low pitch $\beta_{tip} = 10°$ and high pitch $\beta_{tip} = 20°$, as shown in figure 8.

Figure 8: 3D Printed NACA propellers

Each propeller were tested at four different advance ratios. During test, freestream velocity and rotation speed were changed to reach the desired advance ratio. The test conditions for $\beta_{tip} = 20°$ propeller can be found in table 2.

Advance Ratio J	Freestream Velocity (m/s)	Re at $75\%R$
0.20	3	5.3×10^4
0.45	6	4.7×10^4
0.70	9	4.5×10^4
1.00	10	3.5×10^4

Table 2: NACA Propellers Test Matrix

A. Variation with Advance Ratio

Five-component measurement for high pitch NACA ($\beta_{tip} = 20°$) propeller is presented here to illustrate the variation of aerodynamic forces and moments with advance ratio and incidence angle. The results for low-pitch NACA propeller are presented in appendix II for reference. Aerodynamic efforts vary in a similar fashion with advance ratio for the two cases, although at different magnitude, as will be illustrated in part B.

Figure 9 presents thrust and torque measurements at four different advance ratios. Experimental results are depicted with empty dots accompanied by error bar. The solid line

represents numerical results of reduced-order model at corresponding conditions. The calculation was performed to $\alpha_p = 90°$ for each advance ratio case.

At $\alpha_p = 0°$, it is understood that at lower advance ratio the propeller blade section encounters a larger angle of attack, and hence the higher thrust and torque coefficient at low advance ratio. As incidence angle starts increasing, the axial freestream component decreases, the effective advance ratio thus reduces. Consequently propeller thrust and torque coefficients increase with incidence angle α_p. The magnitude of variation depends on the amount of change in axial freestream component, and therefore larger increase in thrust and torque coefficients is observed at higher advance ratio.

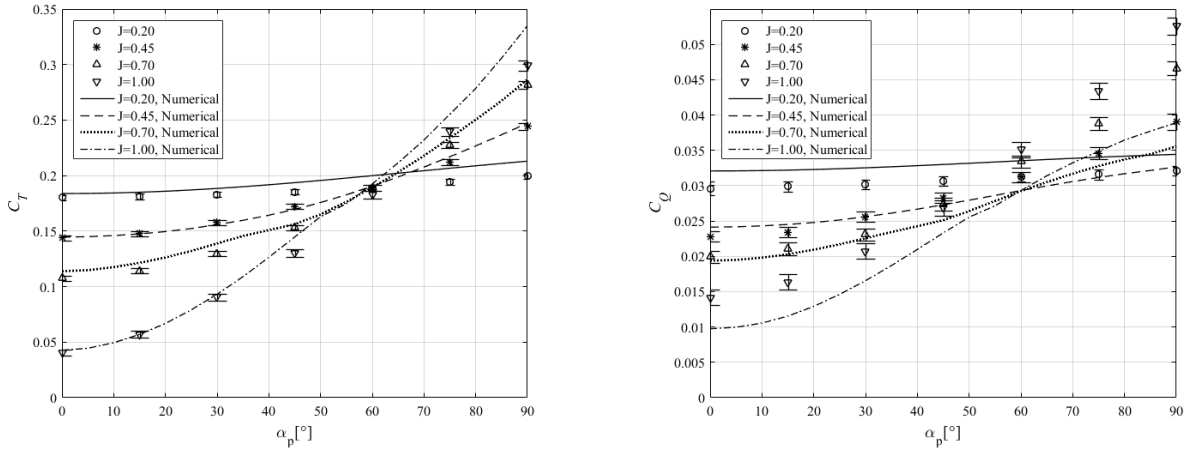

(a) Thrust coefficient C_T

(b) Torque coefficient C_Q

Figure 9: Thrust and torque measurements on NACA propeller with $\beta_{tip} = 20°$

The numerical calculation follows measured thrust well as incidence angle increases. However, larger errors are found in torque coefficient predictions, especially at high advance ratio and high incidence angle.

Asymmetrical loads for high pitch propeller are plotted in figure 10 for normal force and yaw moment, and figure 11 for pitching moment.

The normal force in figure 10 shows a quasi-linear increase in the downstream direction up to $\alpha_p = 60°$, afterwards its rate of increase reduces, and normal force appears to peak at or slightly before $\alpha_p = 90°$.

Yaw moment coefficient exhibits similar trend on the right plot. In axial condition, yaw moment equals zero. As incidence angle increases, the advancing-retreating blade effect produces a moment in the direction from advancing to retreating side of the rotor disk. Yaw moment increases quasi-linearly until non-linear region at high incidence. Both the variations of normal force and yaw moment increase with advance ratio.

The numerical results agree well with the experimental data for both normal force and

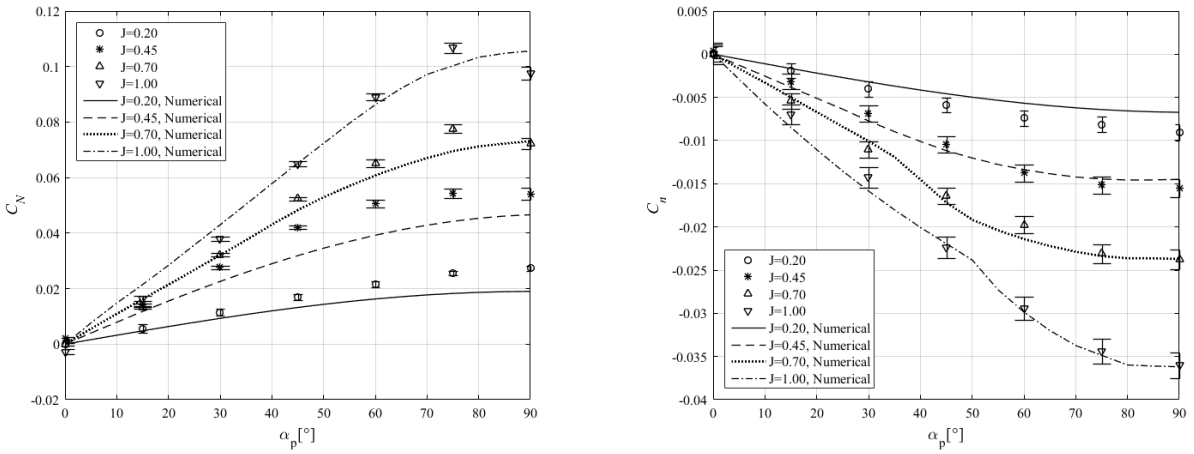

(a) Normal force coefficient C_N

(b) Yaw moment coefficient C_n

Figure 10: Normal force and yaw moment measurements on NACA propeller with $\beta_{tip} = 20°$

yaw moment coefficients. Deviations are mostly observed for high incidence angle.

Figure 11 demonstrates the pitch moment variation at different incidence angle. A small increase in pitch moment can be observed at a maximum value of around 0.01, similar to the maximum yaw moment at $J = 0.2$. Unlike normal force and yaw moment, pitch moment varies little with advance ratio. The mechanism that produces such moment is at least partly because of a distortion in induced velocity field along upstream-downstream direction. By adopting Pitt-Peters inflow model, the numerical results are capable of capture the pitch moment effect to a reasonable degree, although value at high incidence angle may be overestimated.

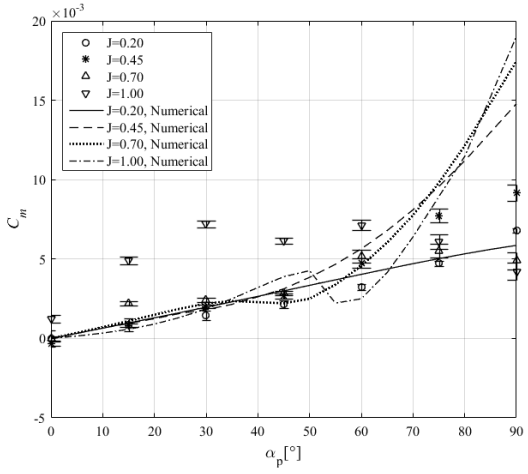

Figure 11: Pitching moment measurements on NACA propeller with $\beta_{tip} = 20°$

B. Variation with Blade Pitch

To understand the propeller performance as a function of pitch angle, the experimental data for both low and high pitch propellers is presented in this section. Only advance ratio $J = 0.45$ is considered. The conclusion is expected to be similar for other advance ratios.

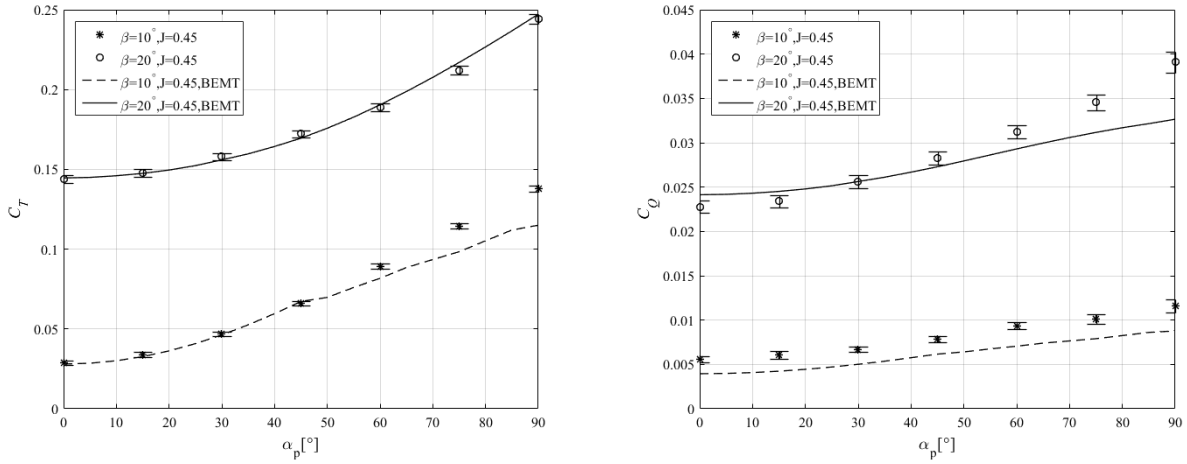

(a) Thrust coefficient C_T

(b) Torque coefficient C_Q

Figure 12: Thrust and torque measurements on two NACA propellers

Figure 12 presents thrust and torque measurements for the two propellers. Open circle symbol represents high pitch propeller and black asterisk is for low pitch propeller. The solid and dash lines are numerical results for the two cases respectively.

For thrust, at $J = 0.45$, a higher pitch propeller produces more thrust than a low pitch propeller, concluded from comparison of thrust coefficient at zero incidence angle. Despite this offset, the variations of thrust coefficient curves the similar.

While producing more thrust, greater torque is required to rotate the higher pitch propeller. The magnitude of peak torque value also appears to be larger for higher pitch angle. This is likely to be caused by a much higher angle of attack achieved on the advancing blade, causing great drag along the direction of rotation. Consequently more power must be supplied to sustain edge-wise flight.

Asymmetrical loads of both propellers are plotted in figure 13 for normal force and yaw moment, and figure 14 for pitching moment.

At this intermediate advance ratio, normal force predictions from calculation underestimates the experimental value for both cases, but the difference are still apparent. The high pitch propeller produces much larger normal force by a factor of 5 compared to the low pitch value. This also supports the theory explaining difference in torque measurements.

Yaw moment measurement gives similar trend with high pitch propeller producing around twice the moment than low pitch propeller. The numerical results captures the difference

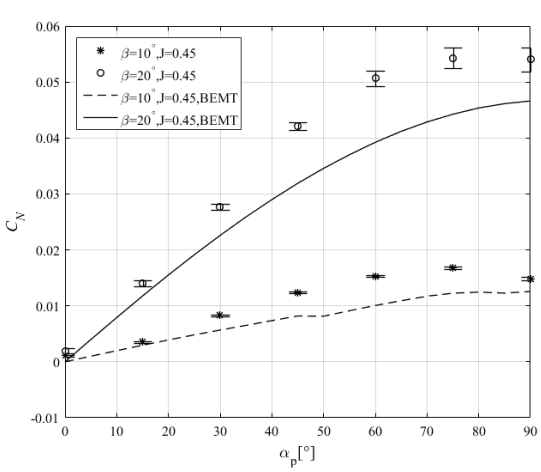

(a) Normal force coefficient C_N

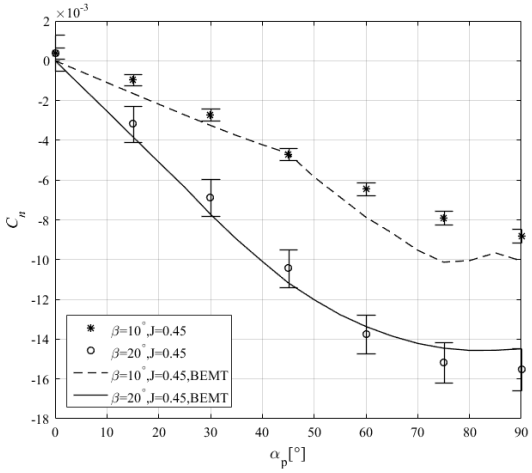

(b) Yaw moment coefficient C_n

Figure 13: Normal force and yaw moment measurements on two NACA propellers

between two pitch settings well.

The comparison of pitching moment for different pitch settings reveals no significant difference. It maybe inferred that pitching moment is of different origin from that of normal force and yaw moment, since those loads are all closely related to flow condition at blade section.

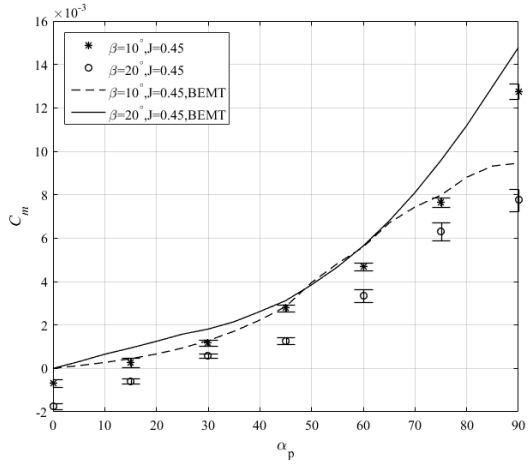

Figure 14: Pitching moment measurements on two NACA propellers

C. Rotational Stall-Delay Effect

During development of the reduced-order propeller model, it was realised that a delay in blade section stall behaviour greatly improves propeller performance at low advance ratio. Such effect is a result of centrifugal and Coriolis effect.[11] The phenomenon is also prominent at high incidence angle around 90°. This can be verified by comparing numerical calculation

with and without stall-delay effect to the experimental result.

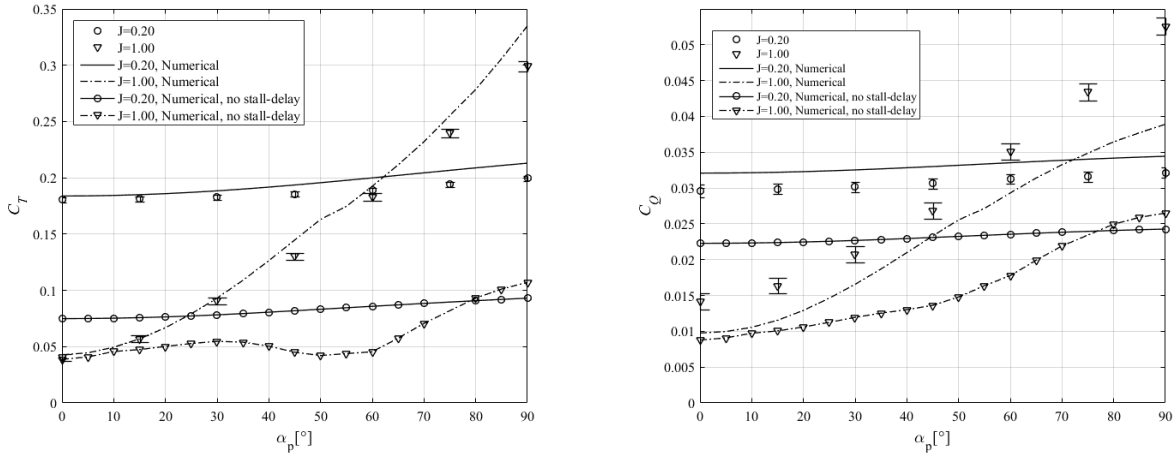

(a) Thrust coefficient C_T (b) Torque coefficient C_Q

Figure 15: Stall-delay effect on thrust and torque

In figure 15 the calculated thrust and torque are plotted for NACA high pitch propeller at advance ratio 0.2 and 1.0. The lines without markers were calculated with stall-delay effect and the marked lines had stall-delay disabled. Corresponding experimental data are also presented for comparison.

At low advance ratio, the effect of stall-delay is apparent. A noticeable underestimation in thrust from experimental data is present at zero incidence with stall-delay effect disabled. The difference continues to increase as incidence angle rises. Most sections of the propeller are presumably stalled, since the increase in incidence angle doesn't cause a corresponding change in thrust at this advance ratio.

For higher advance ratio of 1.0, the effect is negligible for low incidence angle. But as α_p increases beyond 20°, the thrust calculation without stall-delay effect falls below experimental data.

The underestimation in thrust is also accompanied by a smaller torque prediction.

Asymmetrical loads for both propellers are plotted in figure 16 for normal force and yaw moment coefficients.

The normal force and yaw moment coefficients show a similar trend. At low advance ratio, both asymmetrical loads are underestimated. For higher advance ratio, the calculation without stall-delay was able to predict asymmetrical loads at small incidence, but underestimated at higher advance ratio.

The calculation for yaw moment without stall-delay is more problematic as the curves are no longer quasi-linear. Considering thrust calculation in the same case remains nearly constant, this suggests thrust vector is shifting over the propeller disk. This likely indicates

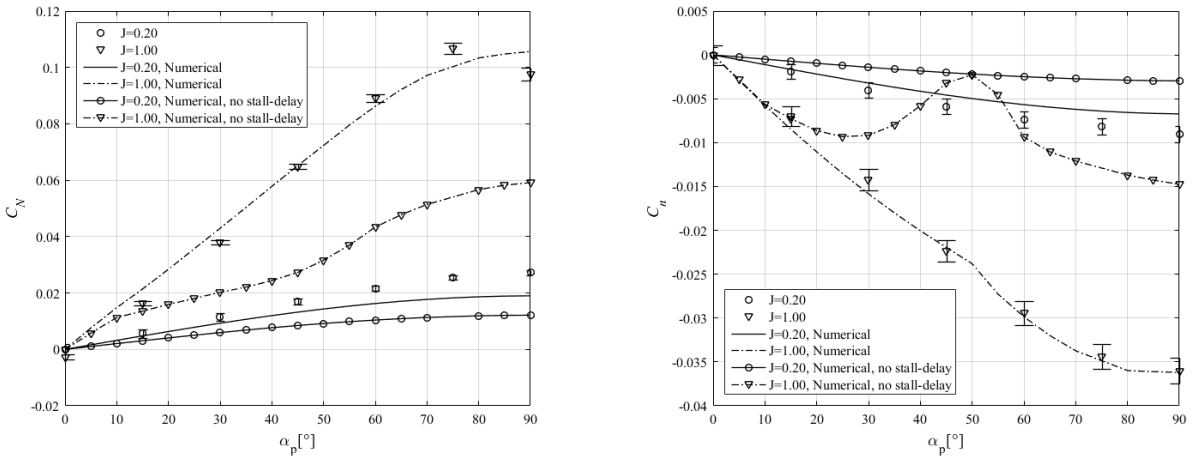

(a) Normal force coefficient C_N

(b) Yaw moment coefficient C_n

Figure 16: Stall-delay effect on normal force and yaw moment

different blade sections stall at varied incidence angle.

V. Conclusion

In this paper, experimental results from a propeller test campaign aimed at investigating incidence angle effect were presented. The test bench at ISAE SaBRe wind tunnel was validated on a propeller in published literature. Tests of 3D printed propellers revealed significant increase in aerodynamic forces and moments at increasing incidence angle. The thrust and torque coefficients increased non-linearly while normal force and yaw moment coefficients showed a quasi-linear increase with incidence angle. Within limits, these effects generally magnify with advance ratio and pitch angle. Pitching moment was found to be a secondary effect with little variation in regard to advance ratio or blade pitch angle.

Validation with reduced-order propeller model suggested reasonable accuracy of such technique applied to preliminary design purposes. Stall-delay effect was identified to be critical in correcting numerical results to experimental value.

References

[1]Itasse, M., Moschetta, J.-M., Ameho, Y., and Carr, R., "Equilibrium transition study for a hybrid MAV," *International Journal of Micro Air Vehicles*, Vol. 3, No. 4, 2011, pp. 229–245.

[2]Lustosa, L. R., Defaÿ, F., and Moschetta, J.-M., "Development of the flight model of a tilt-body MAV," International Micro Air Vehicle Conference and Competition, Toulouse, France, August 2014.

[3]Phillips, W. F., *Mechanics of flight*, John Wiley & Sons, 2004.

[4]Bronz, M., Smeur, E. J., Garcia de Marina, H., and Hattenberger, G., "Development of a Fixed-Wing mini UAV with Transitioning Flight Capability," 35th AIAA Applied Aerodynamics Conference, AIAA AVIATION Forum, Atlanta, United States, June 2017.

[5]Kuhn, R. E. and Draper, J. W., "Investigation of the aerodynamic characteristics of a model wing-propeller combination and of the wing and propeller separately at angles of attack up to 90 degrees," , No. NACA-TR-1263, January 1956.

[6]Yaggy, P. F. and Rogallo, V. L., "A wind-tunnel investigation of three propellers through an angle-of-attack range from 0 deg to 85 deg," Tech. Rep. NACA-TN-D-318, NASA Ames Research Center, Moffett Field, CA, United States, May 1960.

[7]Theys, B., Dimitriadis, G., Hendrick, P., and De Schutter, J., "Experimental and Numerical Study of Micro-Aerial-Vehicle Propeller Performance in Oblique Flow," *Journal of Aircraft*, Vol. 54, No. 3, 2017, pp. 1076–1084.

[8]Theys, B., Dimitriadis, G., Andrianne, T., Hendrick, P., and De Schutter, J., "Wind tunnel testing of a VTOL MAV propeller in tilted operating mode," *2014 International Conference on Unmanned Aircraft Systems, ICUAS 2014 - Conference Proceedings*, 05 2014, pp. 1064–1072.

[9]Hoerner, S., *Fluid-dynamic drag: pratical information on aerodynamic drag and hydrodynamic resistance*, Hoerner Fluid Dynamics, 2001.

[10]Bramwell, A., "Some Remarks on the Induced Velocity Field of a Lifting Rotor and on Glauert's Formula," Current Papers 1301, Aeronautical Research Council, 1974.

[11]Snel, H., Houwink, R., Bosschers, J., et al., *Sectional prediction of lift coefficients on rotating wind turbine blades in stall*, Netherlands Energy Research Foundation Petten, Netherlands, 1994.

Appendix I: Static Mass Error

Due to the displacement of between the balance and motor-propeller centre of mass, there exists a static error in the force and moment measurement. Furthermore, small inclination of the support mast introduces a dependence on propeller incidence angle. A simplified free-body diagram is shown below for the test assembly with exaggerated inclination.

Three coordinates are depicted in the diagram: 1) ground-fixed frame $OX_iY_iZ_i$; 2) intermediate frame $OX_IY_IZ_I$ and 3) balance body frame $OX_bY_bZ_b$ as introduced before. The motor-propeller centre of mass is assumed to be located at z_m and x_m in body frame.

Primary structural deformations are determined to be the inclination of balance frame's X_b and Y_b axes. The diagram below defines the deformations as two angles φ and γ.

The derivation will consider $\alpha_p = 0$ as the baseline case, where, for $\varphi = \gamma = 0$, Z_b axis is parallel to the opposite freestream direction. From the baseline case, the frame first rotates

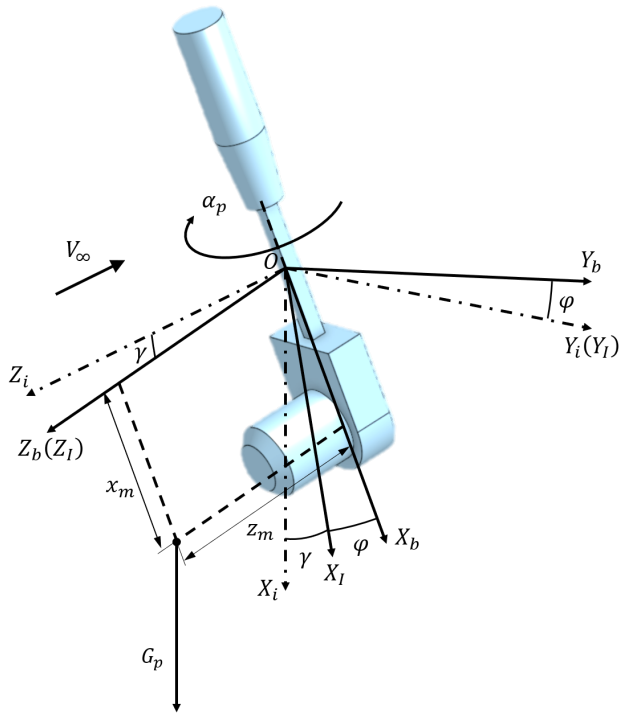

Figure 17: Definition of Balance Inclinations

angle γ around Y_i axis to become intermediate frame $OX_IY_IZ_I$. Then the frame further rotates an angle φ around Z_I axis to reach body frame $OX_bY_bZ_b$. Finally, the body axis rotates around its X_B axis for different incidence angles α_p.

In ground-fixed frame, the motor-propeller assembly gravity force G_p lies entirely in X_i direction.

$$\vec{F}_0^i = \begin{bmatrix} G_p & 0 & 0 \end{bmatrix}^T$$

To obtain the force components in body axis, the force in ground-fixed frame is multiplied by three rotation matrices in order: 1) γ around Y; 2) φ around Z and 3) α_p around X. The resultant static force error can be found below.

$$\begin{aligned} \vec{F}_0^b &= \begin{bmatrix} 1 & 0 & 0 \\ 0 & \cos\alpha_p & \sin\alpha_p \\ 0 & -\sin\alpha_p & \cos\alpha_p \end{bmatrix} \begin{bmatrix} \cos\varphi & \sin\varphi & 0 \\ -\sin\varphi & \cos\varphi & 0 \\ 0 & 0 & 1 \end{bmatrix} \begin{bmatrix} \cos\gamma & 0 & -\sin\gamma \\ 0 & 1 & 0 \\ \sin\gamma & 0 & \cos\gamma \end{bmatrix} \begin{bmatrix} G_p \\ 0 \\ 0 \end{bmatrix} \\ &= \begin{bmatrix} \cos\varphi\cos\gamma \\ \sin\alpha_p\sin\gamma - \cos\alpha_p\sin\varphi\cos\gamma \\ \cos\alpha_p\sin\gamma + \sin\alpha_p\sin\varphi\cos\gamma \end{bmatrix} G_p \end{aligned}$$

To obtain the static moment error, the force error in body frame is multiplied by respective moment arm x_m and z_m.

$$\begin{aligned}\vec{M}_0^b &= \begin{bmatrix} 0 & -z_m & 0 \\ z_m & 0 & -x_m \\ 0 & x_m & 0 \end{bmatrix} \vec{F}_0^b \\ &= \begin{bmatrix} z_m \left(\cos\alpha_p \sin\varphi \cos\gamma - \sin\alpha_p \sin\gamma\right) \\ z_m \cos\varphi \cos\gamma - x_m \left(\cos\alpha_p \sin\gamma + \sin\alpha_p \sin\varphi \cos\gamma\right) \\ x_m \left(\sin\alpha_p \sin\gamma - \cos\alpha_p \sin\varphi \cos\gamma\right) \end{bmatrix} G_p\end{aligned}$$

Thus, neglecting the superscript b for body frame, the static mass error can be modelled as below.

$$\begin{bmatrix} \vec{F}_0 \\ \vec{M}_0 \end{bmatrix} = \begin{bmatrix} \cos\varphi \cos\gamma \\ \sin\alpha_p \sin\gamma - \cos\alpha_p \sin\varphi \cos\gamma \\ \cos\alpha_p \sin\gamma + \sin\alpha_p \sin\varphi \cos\gamma \\ z_m \left(\cos\alpha_p \sin\varphi \cos\gamma - \sin\alpha_p \sin\gamma\right) \\ z_m \cos\varphi \cos\gamma - x_m \left(\cos\alpha_p \sin\gamma + \sin\alpha_p \sin\varphi \cos\gamma\right) \\ x_m \left(\sin\alpha_p \sin\gamma - \cos\alpha_p \sin\varphi \cos\gamma\right) \end{bmatrix} G_p$$

Appendix II: Results for NACA Propeller with $\beta_{tip} = 10°$

Experimental results for low-pitch NACA propeller with $\beta tip = 10°$ are presented in this appendix for reference. Due to the lowered pitch, the test condition was chosen to focus on low advance ratio, as detailed in table 3.

Advance Ratio J	Freestream Velocity (m/s)	Re at 75%R
0.22	3	5.3×10^4
0.29	3	4.2×10^4
0.45	6	5.4×10^4
0.58	6	4.3×10^4

Table 3: Low-Pitch NACA Propeller Test Matrix

The results are presented in a similar fashion as the high-pitch propeller introduced in section IV. The results are presented with BET numerical calculations in solid lines. Thrust and torque coefficients are plotted in figure 18; normal force and yaw moment coefficients are in figure 19 and pitch moment coefficient is shown in figure 20.

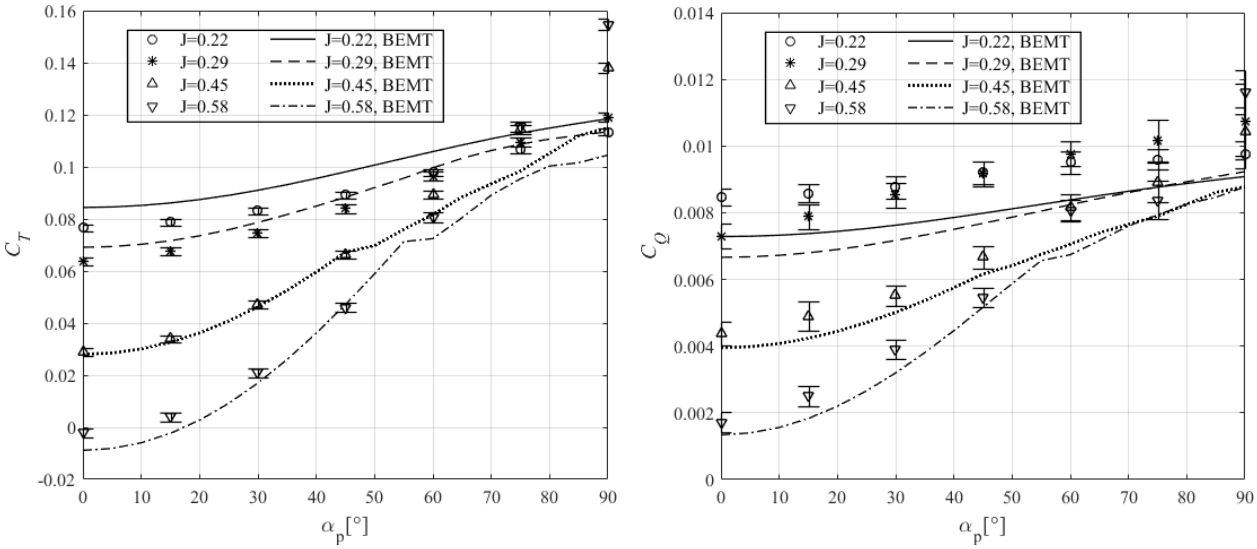

(a) Thrust coefficient C_T

(b) Torque coefficient C_Q

Figure 18: Thrust and torque measurements on NACA propeller with $\beta_{tip} = 10°$

The numerical solution has some noticeable discrepancies in low advance ratio and high incidence conditions. The cause is most likely the modelling of stall delay phenomenon, which is a dominant effect in these conditions. Despite this, the data demonstrated good agreement between the BET method and measurement over broad range of operation similar to transition flight phase of a drone.

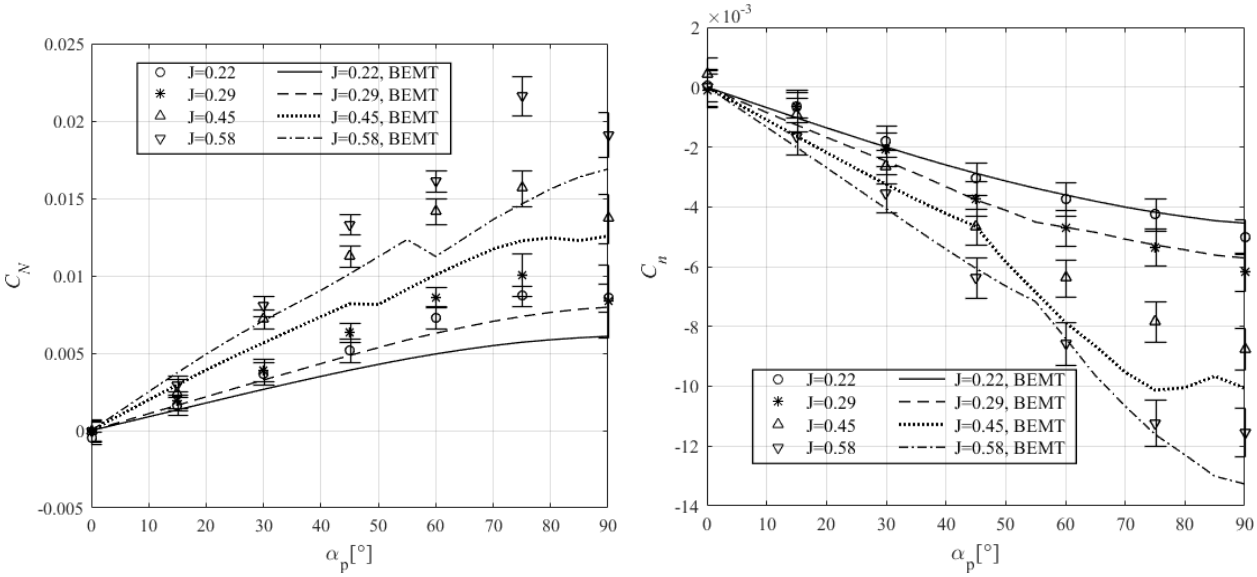

(a) Normal force coefficient C_N

(b) Yaw moment coefficient C_n

Figure 19: Normal force and yaw moment measurements on NACA propeller with $\beta_{tip} = 10°$

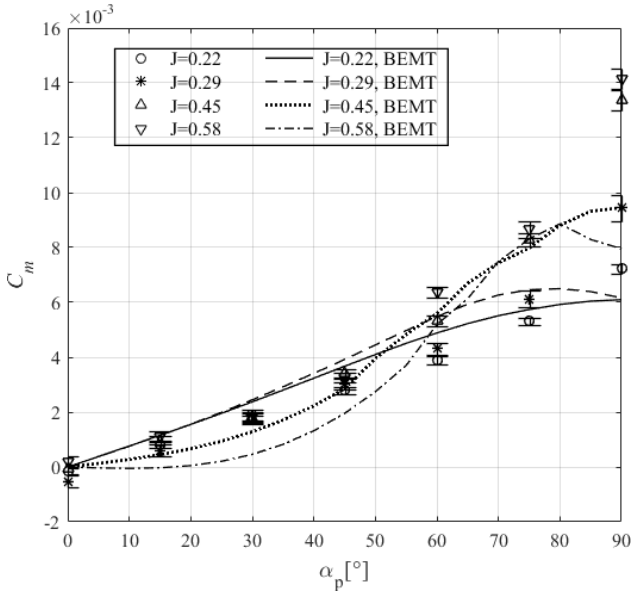

Figure 20: Pitching moment measurements on NACA propeller with $\beta_{tip} = 10°$